Creep mechanisms in the lithospheric mantle inferred from deformation of iron-free forsterite aggregates at 900–1200 °C

Julien Gasc, Sylvie Demouchy, Fabrice Barou, Sanae Koizumi, Patrick Cordier

Creep Mechanisms in the Lithospheric Mantle Inferred from Deformation of Iron-Free Forsterite Aggregates at 900-1200 °C

Julien Gasc[1, 2, 3 *], Sylvie Demouchy[2], Fabrice Barou[2], Sanae Koizumi[4], Patrick Cordier[5]

[1] Centre de Recherches Pétrographiques et Géochimiques, Université de Lorraine and CNRS, UMR 7358, Vandœuvre-lès-Nancy, France.
[2] Géosciences Montpellier, Université de Montpellier and CNRS, UMR5243, Montpellier, France
[3] Laboratoire de Géologie, École Normale Supérieure and CNRS, UMR8538, Paris, France
[4] Earthquake Research Institute, University of Tokyo, Tokyo, Japan
[5] Unité Matériaux et Transformations, Université de Lille and CNRS, UMR8207, Villeneuve d'Ascq, France

*corresponding author: gasc@geologie.ens.fr

Abstract

To further constrain the plasticity of rocks in the uppermost lithospheric mantle, deformation experiments were carried out on forsterite aggregates using a gas-medium apparatus (Paterson press) at 300 MPa, 900-1200 °C and nearly constant strain rates of ~ 10^{-5} s^{-1}. The starting material was a synthetic iron-free forsterite aggregate with an average grain size of ~2.8 μm and ~2-3 % of iron-free enstatite. Eight deformation experiments were performed as well as an additional static annealing to characterize grain growth. The maximum stresses obtained range from ~480 to 1870 MPa. Below 1000 °C, where stress significantly exceeds confining pressure, and based on microstructural observations, grain boundary mediated creep is observed, with evidences of sliding and cavitation (gaping) at grain boundaries. At 1050-1200 °C, where pseudo-steady state could be achieved, the microstructures are very different and show evidences of dislocation activity, resulting from the activation of several dislocation slip systems with increasing temperature.

When compared to rheology laws previously obtained from similar experiments, the temperature dependence of iron-free olivine creep is similar to the one of its iron-bearing counterpart at high temperature (~1200 °C); at temperatures ≤ 1000 °C, however, the strength of iron-free olivine is higher than for iron-bearing olivine. The deformation-induced textures obtained show that grain boundary sliding (GBS) lead to cavitation, which was activated in response to large differential stresses, i.e., beyond the Goetze criterion. Given these high-stress conditions, our results cannot be directly applied to deformation of the Earth's mantle at large scale. Nevertheless, they highlight the key role played by grain boundaries in producing strain at lithospheric temperatures, when crystal-plastic mechanisms remain inefficient.

Keywords: olivine, deformation, grain boundary sliding, upper mantle, high pressure

1. Introduction

The lithospheric mantle can be subject to temperatures as low as 500 °C. Experimental deformation of mantle rocks at such low temperatures is a major challenge in mineral and rock physics, since the strain rates necessary to achieve steady state dislocation creep are too low to be performed in the laboratory. Consequently, deformation experiments that provide insights into the "cold" rheology of olivine, are performed at high stresses without achieving geologically relevant steady state and the strain rate dependence is difficult to assess (Druiventak et al., 2011; Mei et al., 2010). Typically, little to no rate-dependence is observed because it is impossible to activate ductile flow, which leads to seemingly large stress exponent values in the flow law (Druiventak et al., 2011). For decades, the flow law of Evans and Goetze (1979), which uses an exponential expression to account for the Peierls stress control over dislocation motion, has been used to model the low-temperature rheology of the olivine-rich rocks composing the uppermost mantle. Nevertheless, recent experimental studies have shown that the uppermost mantle is likely much weaker than previously expected from extrapolations of high-temperature rheology flow laws to upper mantle temperatures (e.g., Demouchy et al., 2009, 2013, 2014, Boioli et al., 2015a, 2015b; Thieme et al., 2018; Gouriet et al., 2019).

A solution to these issues, is to identify the physical deformation mechanisms at play (e.g., dislocation slip systems) and to implement them in numerical dislocation dynamics models (Boioli et al., 2015a, 2015b, Gouriet et al., 2019). Although this approach gives valuable insights into single crystal plasticity, it does not fully describe the creep behavior of polycrystalline rocks, which may arise from a variety of interacting deformation mechanisms. Therefore, to grasp the complexity and better constrain the low-temperature rheology of mantle rocks, and despite the issues mentioned above, experiments on olivine aggregates are still needed.

The incorporation of iron, hydrogen and titanium in the atomic structure of olivine is known to induce a weakening effect (iron: e.g., Zhao et al., 2009, 2018; Bollinger et al., 2015; Hansen et

al., 2012; hydrogen: e.g., Mackwell et al., 1985; Mei and Kohlstedt, 2000; Tasaka et al., 2016; Tielke et al., 2017; titanium: e.g., Faul et al., 2016; Cline II et al., 2018). To avoid adding complexity to the olivine plasticity due to its dependence upon point defects (i.e., vacancy concentrations), it was thus chosen here to restrict the deformation experiments to hydrogen-free, iron-free fine-grained forsterite-rich aggregates.

We used a two-phase aggregate material, mostly composed of forsterite (with minor amounts of enstatite), which has previously been used in several deformation studies at low pressure and high temperature, in the diffusion creep regime (Tasaka et al., 2013; Nakakoji et al., 2018). The aim of the present study is to assess the creep mechanisms of this fully equilibrated fine-grained aggregate under conditions more relevant to the uppermost mantle, i.e., under significant confining pressure and colder temperatures. In particular, we focus here on a temperature range that encompasses the transition from power law flow (high temperature, $T > 0.6$ Tm, where Tm is melting temperature; for Fo_{100}, Tm=1890 °C) to exponential law flow ("cold" temperature, 0.3-0.6 Tm). In addition to the mechanical data, the microstructures are analyzed with state-of-the-art techniques to provide valuable information regarding deformation mechanisms.

2. Materials and Methods

2.1 Starting material

The samples used in this experimental study were produced from synthetic nano-sized powders at the Earthquake Research Institute (Tokyo, Japan), following a sintering procedure previously described in details by Koizumi et al. (2010), which we only briefly outline here. Starting nano-sized powders of forsterite and enstatite were first synthesized from high purity SiO_2 and $Mg(OH)_2$, then pre-pressed into the desired cylindrical shape in carbide dies, and pressed under hydrostatic conditions at 200 MPa. The resulting cold-pressed specimens were then annealed under

vacuum at 1260 °C for 2-3 hours, which yields a fully dense aggregate (< 1 % porosity) and ensures complete dehydration (Koizumi et al., 2010). The chemical composition of the starting material was analyzed by X-ray fluorescence with a Philips® PW 2400 spectrometer (see Supp. Mat. Table S1). Iron content is under 10 ppm. This new type of high-quality sintered aggregate has proven to be an excellent material for rheology studies (Hiraga et al., 2013; Tasaka et al., 2013). The microstructure of the starting material was characterized by scanning electron microscopy (SEM) and electron backscatter diffraction (EBSD). The EBSD map in Figure 1 shows that the bi-minerallic aggregate is composed of pure forsterite with an average equivalent diameter of 2.8 μm. It also contains ~2-3 % of orthoenstatite homogeneously distributed across the aggregate with a smaller grain size than forsterite (1.8 μm on average), which prevents it from impacting the bulk rheological properties (Huet et al., 2014; Ji et al. 2001). The EBSD maps also provide statistical data on the microstructure, as reported in Table 1. The starting material shows equilibrated textures, with ubiquitous triple junctions and straight grain boundaries (Figure 1), as already described by Koizumi et al. (2010). Due to the very fine grain size, initial porosity is difficult to assess from SEM images since it is difficult to differentiate between actual residual pores from sample sintering and newly formed cavities caused by grain plucking during cross section preparation. Nevertheless, porosity has been characterized in previous studies and is estimated to be significantly less than 1 % in volume (Koizumi et al., 2010). As observed on Figure 1, the grains are nearly equiaxed. Their aspect ratio is found here to be 1.9, whereas previous studies using the same material have reported a value of 1.3-1.4 (Koizumi et al., 2010). The aggregate starting material has a measurable shape preferred orientation (SPO), most likely inherited from the cold press stage of the samples synthesis (Koizumi et al., 2010). The samples used for deformation consisted in cylinders with diameters ranging from 4.5 to 4.8 mm, and lengths varying between 7.25 and 10.55 mm (Table 1).

2.2. Deformation experiments

Eight deformation experiments were carried out using a high-resolution gas-medium high-pressure high-temperature apparatus (Demouchy et al., 2013, 2014; Paterson, 1990, Thieme et al., 2018) at Geosciences Montpellier (University of Montpellier, France). An additional static annealing test was carried out without deformation to assess the importance of grain growth during our experiments (NF_1000-0, Table 1). All experiments were performed under a confining pressure of 300 MPa using argon gas. Constant piston-displacement uniaxial deformation was performed under constant temperatures ranging from 900 to 1200 °C (Table 1). The samples were placed between alumina and zirconia pistons and fitted in metal sleeves (e.g., Mei and Kohlstedt, 2000; Demouchy et al., 2014). The nature of the metal sleeve was chosen depending on the temperature of each experiment, to avoid melting of the sleeve while keeping its strength as low as possible (Table 1). Silver, copper and nickel sleeves were used for experiments at <1000 °C, 1000-1050 °C, and >1050 °C, respectively (Table 1). All parts were encapsulated in an iron jacket thin enough to transmit the confining pressure.

Axial force values were obtained from an internal load cell during deformation. Flow laws for Cu, Fe, Ni, and Ag from Frost and Ashby (1982) were used to determine the contributions of the iron jacket and the metal sleeve to the measured load. Sample stress as a function of time was then retrieved by calculating the evolution of the sample surface corresponding to a shortening with constant volume. Strain was corrected using the apparatus stiffness, which was calibrated beforehand (~83 kN mm^{-1}). The stress-strain data were further processed (smoothed) to accurately identify the yield point and the apparent Young moduli at yield point (see Supp. Mat. for details, Figures S1 and S2).

For each experiment, constant displacement rate was set based on the initial length of the sample to yield a stress plateau with a strain rate of 10^{-5} s^{-1}. All samples were deformed, at least, until the maximum stress was achieved. Below 1050 °C, axial shortening was stopped if a significant stress decrease—indicative of brittle failure of the sample—was observed. At temperatures

137 > 1050 °C, a plateau with constant stress was obtained and more extensive deformation was
138 performed. Finite strain ranged from 2.8 to 12.4 % (Table 1).

139

140 **2.3 Scanning electron microscopy and electron backscattered diffraction**

141 The recovered samples were kept in the metal sleeve and jacket and cross sections were cut
142 either normal or parallel to the compression direction for SEM and EBSD. The sample sections
143 were prepared using a standardized polishing protocol (Thieme et al., 2018). A final chemo-
144 mechanical polishing step using colloidal silica on a vibrating plate was necessary to achieve a high-
145 quality polish for EBSD. The SEM and EBSD analyses were performed with a CamScan X500FE
146 Crystal Probe equipped with an EBSD system at Geosciences Montpellier (University of
147 Montpellier, France). The geometry of the Crystal Probe-EBSD was previously detailed in
148 Demouchy et al. (2011). Operating conditions were 15-18 kV, ~6 or 10 nA (for exposure times of
149 48 and 24 ms, respectively) and a working distance of 24-25 mm. Low vacuum conditions (4 Pa of
150 gaseous nitrogen), carbon coating and copper-carbon tape were used around the studied area to
151 avoid charging of the specimen. Several EBSD maps were collected on each sample section,
152 including on the starting material (undeformed), as well as on the statically annealed sample.

153 The dimensions of the area mapped by EBSD typically varied from a few tens to several
154 hundreds of microns, which corresponds to hundreds to several thousands of grains, thus allowing
155 satisfying statistical analysis in terms of grain size, shape grain and crystallographic orientation. The
156 step size was set either to 0.2 or 0.4 μm depending on the size of the analyzed area.

157 The data were acquired using Oxford instrument's HKL Aztec2 software. Data were first
158 processed to remove wild spikes (isolated pixels that have eight similar neighbors) and fill non-
159 indexed pixels that had seven neighbors with identical orientations, then treated with the MTEX
160 MATLAB toolbox (Bachmann et al., 2010; Hielscher and Schaeben, 2008; Mainprice et al., 2015).

Grain boundaries are usually detected using a critical misorientation angle of 10-15° (Mainprice et al., 2015). Here, grain boundaries were detected using a threshold misorientation angle of 13°. Variations of this critical threshold angle between 10 and 15° does not impact the microstructure results significantly (see Supp. Mat., Table S2). Grains were filtered to a minimum of 1.44 μm^2 (i.e., 9 or 36 pixels, according to the step size). Similarly, subgrains were identified as neighboring pixels with misorientations of 2-13°. The density of the orientation distribution function was calculated using an axially symmetric de la Vallee Poussin kernel, with a half-width of 10° (bandwidth of 28 in spherical harmonic coefficients). Crystal preferred orientations (CPO) and texture J-index were calculated (Bunge, 1982). The texture J-index is a measurement of the texture strength calculated as the integral of the square of the orientation distribution function, and is calculated using one data point per grain to avoid overestimating the contribution of large grains (Mainprice et al., 2015). Densities of pole figures were normalized to a uniform distribution and contoured at intervals of 0.06 × uniform.

2.4 Transmission electron microscopy

Transmission electron microscopy (TEM) was also used to characterize the microstructures after the deformation experiments. Three deformed samples (NF_950-1, NF_1050-1 and NF_1200-1) were selected for this investigation from which doubly polished thin sections (30 μm thick) were prepared. Sample NF_1200-1 was cut parallel to the deformation axis, and NF_950-1 and NF_1050-1 perpendicular to the deformation axis. They were glued on a Cu grid and ion milled at 5 kV under a low beam angle of 15° until electron transparency was reached. The foils were subsequently covered with a thin layer of carbon. TEM observations were carried out at the University of Lille (France) using a FEI® Tecnai G2-20 TWIN microscope operating at 200 kV.

185 **3. Results**

186 **3.1 Mechanical data**

187 The stress-strain curves from each deformation experiment are shown in Figure 2. Stress data
188 for experiment NF_1110-1 appear noisier than other experiments due to a temporary grounding
189 issue of the internal load cell during the deformation, which resulted in apparent stress fluctuations
190 (Figure 2a). Maximum stresses range from 480 to 1870 MPa, for temperatures varying from 1200
191 to 900 °C, respectively. The mechanical values reported in Table 1 thus define an expected inverse
192 dependence with increasing temperature. At temperatures ≤1000 °C, stress increases until it
193 reaches a maximum, then starts decreasing upon further straining. Sample failure was observed for
194 NF_900-1. For experiments NF_950-1, NF_1000-1 and NF_1000-2, deformation was stopped
195 after observing a significant stress decrease, indicative of possible imminent failure. In contrast, at
196 higher temperatures (>1000 °C), stress reaches a constant value (plateau) and samples could be
197 further deformed in an apparent (quasi-) steady state. We note however, that, for all experiments,
198 the stress increases above the confining pressure (> 300 MPa) and is upheld without immediate
199 failure over non-negligible amounts of strain, i.e., several percent after apparatus stiffness
200 correction.

201 From 900 to 1110 °C, yield stress values are close to ~600 MPa, regardless of temperature.
202 Yield stress is only significantly lower in experiment NF1200-1, performed at the highest
203 temperature (Figure 2b). In contrast, aside from experiment NF1110-1, we observe a consistent
204 decrease in the apparent Young modulus with temperature, from 112 GPa at 900 °C to 32 GPa at
205 1200 °C (Table 1).

206 **3.2 Microstructures**

207 Results from EBSD analyses on the deformed aggregates are summarized in Table 1. Average
208 grain size, aspect ratio and shape factor (i.e., measured perimeter/perimeter of the circle with

209 equivalent area) values obtained for the largest map in each sample, are shown as a function of
210 finite strain and temperature in Figure 3. For the sake of readability, a full statistical report is
211 provided in the supplementary material, where results from the two largest maps for each sample
212 are given along with corresponding minimum, maximum and standard deviation values (Table S3).
213 We note that values of aspect ratio are somewhat larger than expected. This is attributed to a slight
214 drift of the electron beam (often observed when working with non-conductive samples) when
215 collecting EBSD maps, which results in a minor artificial elongation of the grains.

216 From the EBSD maps, average grain sizes of 2.7-3.3 μm are found. Therefore, both in the
217 static annealing test NF_1000-0 and in the deformation experiments, grain size remains essentially
218 unchanged from the value measured in the starting material. Only a slight decrease (–15 %) in grain
219 size is observed in the deformed samples (Table 1, Figure 3). Nevertheless, one finds no correlation
220 between grain size and temperature or strain over the entire data set (Figure 3), consistently with
221 the results of Tasaka et al. (2013), who reported only minor grain growth, even at temperatures as
222 high as 1260 °C. Based on the low temperatures and short durations of the present experiments,
223 static growth is therefore negligible here (Table 1, Figure 3).

224 SEM images displayed in Figure 4, show the preservation of equilibrium texture features, such
225 as triple junctions and straight boundaries in the samples deformed at 950-1000 °C. Visually,
226 textures from samples deformed more extensively and at greater temperatures (1050-1200° C)
227 show more curved grain boundaries (Figure 4g, h). This is confirmed by the values of shape factor
228 and aspect ratio, which remain essentially unchanged, when compared to the starting material, for
229 the samples deformed at 900-1000 °C, as well as for NF1110-1 (all of which experienced less than
230 10 % strain), but are slightly larger for the three samples deformed by at least 10 % strain at 1050-
231 1200 °C (Table 1, Figure 3). In the low-temperature samples, many grain boundaries are open
232 (Figure 4), a feature that seems much less common at 1000-1110 °C and which is not observed at
233 1200 °C.

In addition, at low temperature, many grains appear with strong topology in the SEM images (Figure 4b), which is due to out-of-plane motion (vertical offsets) between adjacent grains in the imaged plane. At 1050 °C, voids created by the opening of grain boundaries are still observed. Typical cases where grains have slid relative to each other and created a void due to insufficient ductility of adjacent grains can be seen in Figure 4d.

In all samples deformed at 1050 °C and 1100 °C, grain boundaries are serrated in a pervasive way as shown in Figure 4. At 1050 °C, the scale of the serration (its wavelength) is at the limit of the observation capability of the SEM, i.e., in the order of tens of nanometers, at most. We note that, due to the relatively small scale at which this change occurs, it is not measurable in terms of shape factor (which increases with grain boundary tortuosity, Figure 3) since EBSD data are collected with much larger step sizes than the serration scale. Nevertheless, the wavelength of the serration seems to increase with temperature and decreasing stress; as also suggested by TEM images of samples NF_950-1 and NF_1050-1 (see below for details). At 1110 °C, the samples show no evidence of major grain boundary sliding but the serration of grain boundaries is ubiquitous and occurs at the scale of a few tens to hundreds of nanometers. Several large grains exhibit important intracrystalline contrast variations, typical of subgrain boundaries (Figure 4f). This results from distortions of the crystal lattice and/or from defect concentrations and therefore highlights active intracrystalline plastic deformation. At 1200 °C, all grain boundaries remained closed and many display incipient bulging, with wavy boundaries at the scale of hundreds of nanometers to a micron (Figure 4h). Neither gaping, nor grain boundary sliding is observed.

The distribution of the long-axis direction of the grains is shown in Figure 5. A strengthening of the initial SPO (i.e., present in the undeformed sample) is observed upon deformation (Figure 5 and Table S3). Indeed, the long-axis of the grains tend to align normal to the compression axis, which is the same as during the compaction stage of the samples, prior to sintering. We note that for samples NF_1110-1 and NF_1110-2, shortened by 12.4 and 5 %, respectively, the long axis

orientation distribution is very similar, which implies that most of the SPO formed during the early stages of the axial deformation.

By definition, grain orientation spread (GOS) defines the variations in local crystallographic orientation inside a given grain. Therefore, in an ideal unstrained crystal lattice, GOS is theoretically nil and its actual value only reflects EBSD measurement uncertainty. This is the case for the undeformed samples, which have an average GOS of 0.2-0.21° (Table 1 and Figure 3). Larger GOS values can reflect plastic deformation due to the presence of internal strain heterogeneities of the crystal lattice, which can originate from residual elastic strains (although unlikely here, in the case of a free surface) or more generally from the presence of geometrically necessary dislocations (GND). In the EBSD maps, GOS increases with the amount of strain to reach a maximum of 1.375° at 1100 °C. The largest values are obtained for samples NF_1110-1 and NF_1050-1 (Figure 3), which reveal substantial intracrystalline plasticity. At higher temperature, increasing temperature seems to have the opposite effect since lower values of GOS (0.705°) were obtained for sample NF_1200-1, deformed by about the same amount (Table 1). A comparison between two EBSD maps collected on samples that have experienced different temperatures and finite strains is shown in Figure 6. Similar to undulose extinction in optical microscopy, Misorientation-to-Mean (Mis2Mean), which represents angular variations in crystal orientation inside a grain relative to the grain's average crystallographic orientation, allows the spatial strain heterogeneity distributions of the crystal lattice to be visualized. When finite strain is the largest, Mis2Mean values, and therefore GOS, often exceed 5°, as evidenced by the brighter areas in Figure 6b, Mis2Mean values > 5° are more common in coarser grains, where subgrains often formed. We note that, in Figure 6a, yellow-saturated grains are a consequence of neighboring grains being incidentally positioned in crystallographically close orientations and therefore identified as single grains with large Mis2Mean values, whereas the actual maximum value is ~1°.

283 Pole figures obtained for the starting material, the annealing test and the deformation
284 experiments are displayed in Figure 7 and show near-random crystal orientations, as pointed out
285 by their very low *J*-indexes ranging from ~1.01-1.11. However, in many cases, analysis over a large
286 number of grains (> 10,000) detected slight but meaningful deviations from a random distribution.
287 As expected, the starting material shows no significant CPO. Samples deformed from 900 to
288 1000 °C experienced small amounts of finite strain and do not show any significant CPO either.
289 Only sample NF_950-1 displays a possibly meaningful pattern, where the [001] axis forms a girdle
290 normal to the compression axis. This very weak CPO pattern may also be present in other samples
291 but was probably only detected in NF_950-1 due to the large EBSD map size, which allowed better
292 statistics (over 14,000 grains analyzed). We note, indeed, that *J*-indexes are consistently higher for
293 smaller EBSD maps, which is an artifact of poorer statistics generating greater local maxima. In
294 the present case, the very weak texture described above was likely present in the sample prior to
295 deformation and preserved due to very low finite strain.

296 In contrast, three out of four samples deformed between 1050 and 1200 °C (≥ 10 % strain),
297 NF_1050-1, NF_1110-1 and NF_1200-1, show a weak CPO characterized by an alignment of the
298 [010] axis parallel to the compression direction. The distribution of [001] axes defines a girdle
299 normal to the shortening direction in NF_1050-1, whereas it displays maxima at ~45° of the
300 shortening direction in NF_1110-1, and is nearly random for NF_1200-1. Similarly, [100] axes have
301 local maxima at 45° of the compression direction in NF_1050-1 and NF_110-1. We note that these
302 features appear fainter for sample NF_1200-1. In addition, this CPO is not observed for sample
303 NF_1110-2, which, consistently with its low finite strain, shows a texture similar to that of the
304 starting material and the low temperature samples.

305 In summary, deformation-induced CPOs are characterized by a concentration of [010] axes
306 parallel to the compression direction, while the other axes tend to form girdles and point maxima,
307 which are normal and at ~45° with respect to the compression direction, respectively. These

patterns are characteristics of the A-fiber texture, where the [100] and [010] axes are parallel to the shearing (lineation) and principal stress directions, respectively (Mainprice et al., 2005; Michibayashi et al., 2016; Ohuchi et al., 2015; Tommasi et al., 2000). Similar textures have also been reported for iron-bearing olivine using the same experimental setup at 900 °C and are indicative of co-existing [100](010), [001](010) and possibly [001]{110} slip systems (Demouchy et al., 2009; Demouchy et al., 2014; Phakey et al., 1972; Raleigh, 1968).

Intracrystalline plasticity was identified in the EBSD maps of the deformed samples via the analysis of misorientation within the grains determined by MTEX. At 1050-1200 °C, many subgrains were observed (misorientations of 2-13°) and statistics on those subgrains could be extracted (Figure 8, Figures S3 and S4). At 900-1000 °C, however, little intragranular plasticity and few subgrains are present. Intracrystalline plasticity was therefore investigated by analyzing targeted grains that showed a GOS > 1° and where deformed areas larger than 10 pixels could be analyzed (Figure 8 and Figure S5). Subgrains can form twist or tilt walls in the grains. Figure 8 (and Supp. Mat. Figures S3 and S4) illustrates the types of subgrains identified in all three samples that have experienced major deformation; i.e., NF_1050-1, NF_1110-1 and NF_1200-1. Subgrains are mostly found in large grains (>~4 μm) and correspond to modest misorientations, typically lower than 5° (Figure S3). Detailed analysis reveals that the majority of subgrain boundaries are tilt walls, i.e., with the rotation axis oriented nearly parallel to the subgrain wall. The most common subgrain types for those three samples (deformed at 1050-1200 °C) are illustrated in Figure 8, where the distribution of subgrain rotation axis is plotted in inverse pole figures. These plots reveal clustering mostly around the [001] and $[\bar{1}10]$ directions. Subgrain rotation around $[\bar{1}10]$ is more prominent at 1050 °C than at 1110 and 1200 °C. At 1200 °C, subgrain rotations around the $[\bar{1}10]$ direction are negligible and rotations around [001] dominate, associated with a slightly larger contribution from subgrain rotations around the <0kl> directions and around the [010] axis.

At 900-1000 °C fewer grains were analyzed. It is therefore difficult to identify specific rotation axes as clearly as in the high-temperature samples (Figure S5). However, a similar trend is observed, particularly for larger misorientation values (which present a lower uncertainty), with rotation axes located near the $[\bar{1}10]$ and [011] directions. We note that, unlike at 1050-1200 °C, those latter rotations seem to be favored over those around the [001] axis.

At 1050-1110 °C, the high concentration of subgrain rotations around [001] probably reflects the appearance of tilt walls as a result of dislocations of screw and edge character in the [001](010) and [100](010) slip systems, respectively, consistently with the CPOs described above. However, other rotations, such as those around $[\bar{1}10]$ and $[011]$ observed throughout the entire 900-1200 °C temperature range investigated (Figures S3 and S4), may simply reflect the presence of GNDs. Those rotations can result from [001]{110} and [100]{011} dislocations, as already identified in previous studies (Cordier et al., 2014; Demouchy et al., 2014; Thieme et al., 2018; Wallis et al., 2016). Conclusively, misorientation may be used as a proxy for dislocation density in general, but does not necessarily represent the density of mobile (free) dislocations accommodating most of the strain.

The three samples investigated by TEM exhibit very distinctive microstructures, as shown in Figure 9. At 950 °C (NF_950-1), consistently with the stress drop observed at high stress, one observes mostly indication of a brittle response (Figure 9a). Although some intragranular microcracks can be occasionally observed, brittleness results predominantly from grain boundary cracking as seen in Figure 9b. In most cases, the grain boundary microcracks are straight and cleavage-like. However, some exhibit serration, suggesting a different behavior before rupture (Figure 9b, Figure S6a), characteristic of ductile cracks (Ponson et al., 2013). The intragranular microstructure is very heterogeneous. Many grains are pristine, but dislocation activity can be observed in some grains, probably related to microplasticity (i.e., plastic deformation by dislocation motion occurs locally, while the bulk material remains essentially in the elastic/brittle field).

357 At the highest temperature investigated (NF_1200-1), the microstructure is also very
358 heterogeneous (Figure 9). Several grains are still dislocation free, however clear dislocation activity
359 is observed in many of them and, consistently with SEM observations, the grain boundaries are
360 perfectly cohesive (Figure 9h, Figure S6d). The most striking observations come from the sample
361 deformed at 1050 °C (NF_1050-1). Very marked grain boundary openings are ubiquitous
362 (Figures 9c-f). Contrary to NF_950-1, damage at grain boundary does not result from purely brittle
363 cleavage-like micro-fracturing. The shape of surfaces formed by crack opening clearly suggests
364 some ductile processes (Figure 9e, Figures S6b and S6c). As a result, some cohesion could be
365 maintained during crack opening. This is probably what explains the ductility exhibited by this
366 sample despite very strong damage. Another characteristic of this sample is the presence of
367 dislocation activity in almost all grains (Figure 9f), which is consistent with the GOS evolution
368 observed among samples (Figure 3). Although dislocation activity might be related to the ductile
369 processes suggested by the crack morphologies, no clear correlation could be evidenced.

370

371 **4. Discussion**

372 **Brittle to ductile transition mechanisms**

373 Between 900 and 1000 °C, no steady state could be achieved (Figure 2). Stress almost
374 immediately reached a yield point, beyond which deformation occurred in a semi-brittle manner,
375 via micro-cataclastic processes (intergranular cracks and sliding). As shown by the images of
376 recovered samples (Figures 4 and 9), for this range of temperature, the stress drop observed beyond
377 the stress maximum likely corresponds to the coalescence and propagation of pervasive micro-
378 crack networks. In the brittle field and across the brittle-ductile transition here, when grains slide
379 relative to each other (GBS), strain incompatibilities develop (usually at triple junctions), which can
380 lead to the formation of voids. In some cases, these voids further develop under local tensile
381 stresses and fully open grain boundaries (Figure 4, Figure 9d). Although these openings can be seen

as mode-I cracks in the brittle sample at 900 °C, an involvement of ductile processes in their development is clearly identified at 950-1110 °C (Figures 4 and 9d,e), where they therefore correspond to "ductile cracks" (Idrissi et al., 2016; Ponson et al., 2013). The presence of pervasive gaping grain boundaries indicates indeed that deformation involved a significant contribution of GBS at the sample scale (Ree, 1994, Langdon, 2006). This is well illustrated by the relative motion of grains in Figure 4d and Figure 9c. The damage (i.e., cavitation) caused by this mechanism is a direct consequence of the moderate confining pressure conditions (0.3 GPa) relative to stress levels and the low temperature (~0.54-0.59 × Tm for Fo_{100}), which, for our experimental durations, prevents diffusion from filling the areas in tension as the grains are pulled apart (e.g., Ree, 1994). Indeed, creep by diffusion would occur if characteristic diffusion lengths were greater than the grain size of the aggregate. This criterion can be assessed using Si diffusivity since it is the slowest diffusing species in silicates. For 900-1000 °C, data from Fei et al. (2012) predict lattice diffusivities of 1.4×10^{-25} to 3.7×10^{-24} m^2 s^{-1} and corresponding characteristic diffusion lengths of ~0.07 to 0.3 nm for the durations of our experiments, which excludes a significant contribution from diffusion creep (e.g., Nabarro-Herring creep). Additionally, theoretical strain rates for diffusion creep can be calculated from the diffusion coefficients mentioned above and using the maximum (or steady-state) stress measured for each experiment (Raj and Ashby, 1971; Tasaka et al., 2013). Using a grain size of 3 μm, representative of our samples, these calculations yield strain rates of the order of 10^{-13}-10^{-10} s^{-1} and therefore confirm the unlikely dominance of diffusion creep in our experiments.

Interestingly, these low-temperature samples (< 1000 °C) sustained major strain hardening without reaching failure and largely exceeded the Goetze criterion, i.e., differential stress exceeded confining pressure (Kohlstedt et al., 1995). Transient violation of the Goetze criterion has been previously reported in similar deformation experiments on fined-grained iron-bearing olivine (Demouchy et al., 2009, 2014; Thieme et al., 2018). In the present case, the Goetze criterion should

only be seen as a condition that predicts the nucleation of cracks (i.e., cavitation), but without necessarily resulting in macroscopic failure.

Interestingly, SEM images of our low-temperature samples show more pronounced surface relief than samples deformed at > 1100 °C (Figure 4b). These features are very similar to the out-of-plane grain displacements on free surfaces reported by Bollinger et al. (2019) at 3.5-5 GPa (1000-1200 °C, 2×10^{-5} s^{-1}), as well as to those evidenced on samples deformed by GBS creep at 1 atm (Watanabe et al., 1982; Maruyama and Hiraga, 2017a, 2017b; Masuda et al., 2015, 2016). Although, the physical explanation for the appearance of these displacements on free-surfaces created after the experiments remains elusive. It is suspected that this late relative grain motion occurs as a relaxation process at grain boundaries in response to large residual stress heterogeneities due to stored elastic energy. This relaxation is made possible by the decohesion of a significant fraction of the grain boundaries. The present study and those of Maruyama and Hiraga (2017a) and Bollinger et al. (2019) thus show the possible activation of GBS under a wide range of confining pressure (0.3-5 GPa). We argue that, under relatively low temperature, rapid laboratory stain rates generate heterogeneous stress concentrations, which can locally be at least equal to the confining pressure, even under several gigapascals of pressure (Druiventak et al., 2011; Burnley, 2013). These stress concentrations either create openings (cavitation), as in our case, or, at high temperature, drive ionic diffusive fluxes towards low-pressure areas (e.g., Wheeler, 2018).

Grain boundary mediated deformation at low strain

The apparent Young moduli (Figure 2b, Figure S2) provide valuable information about the deformation behavior of the aggregates at low strain. Both yield stresses and corresponding apparent Young moduli are reported in Figure 10 as a function of temperature. Our results describe a linear temperature dependence of –263 MPa/°C. This value is too large to be explained by forsterite elasticity only, as shown by the comparison with the values of Suzuki et al. (1983), which yield a temperature derivative of –32 MPa/°C (Figure 10a). These results corroborate the recent

study of Burnley and Kaboli (2019) on iron-bearing olivine aggregates. It is unclear what percentage of the strain is accommodated elastically or plastically at this stage of the deformation curves. This deviation from purely elastic behavior observed upon modest amounts of strain may reflect a contribution of GBS, accordingly with TEM images, which evidence an involvement of ductile processes in the grain boundary network. In any case, these data suggest a major rheological impact of the grain boundaries with increasing temperature. Since grain boundary mediated deformation is activated at lower temperatures than crystal plastic mechanisms, it may play a key role in the mantle at low temperature and/or high stress conditions, typical of the brittle-ductile transition.

Flow mechanisms and comparison to previous rheological laws

In the 900-1000 °C range, there is no deformation-induced CPO pattern (Figure 7), accordingly with the low amounts of strain experienced by the samples. At the TEM scale, dislocation activity is observed in NF_950-1, but is likely related to microplasticity, and coexists with pervasive microfracturing (Figure 9a). As discussed above, in this temperature range, deformation is transiently ductile at the sample scale, and shortening results from the propagation of micro-cracks at the grain (micrometric) scale, together with minor dislocation activity (glide of [100] and [001] dislocations), as previously proposed by Druiventak et al. (2011). Consequently, the maximum stresses obtained in this temperature range correspond to a semi-brittle regime and lie largely above previously established low temperature flow laws, as shown in Figure 11. We note, as pointed out by previous studies (e.g., Demouchy et al., 2009, 2013, 2014, Thieme et al., 2018), that extrapolations from power law flow yield overestimated stress values for the present temperature range and strain rates.

At, or above, 1050 °C, apparent steady state was achieved over the strain range investigated (Figure 2) and two observations stand out: (1) GOS values are the highest at 1100 °C, then decrease at 1200 °C (Figure 3). Therefore, the increase in GOS from 900 to 1100 °C, associated with the

appearance of numerous subgrain boundaries (Figure 8), reflects an increasing contribution of intracrystalline plasticity with temperature, whereas the lower value obtained at 1200 °C likely indicates a contribution of diffusive mechanisms. (2) In addition, grain boundary sliding, opening and serration are also commonly observed (Figure 4, and Figures 9c-e), indicative of grain boundary mediated plasticity. Thus, deformation in the 1050-1110 °C range corresponds to a transitional regime where both plastic and cataclastic deformation mechanisms are active.

At 1200 °C, a quasi-steady state is achieved rapidly, after only 3 % of strain. The microstructure is noticeably different, with almost no grain pluck out, no evidence of grains sliding relative to each other, no out-of-plane motion, and less grain boundary serration, when compared to samples deformed at 1050 and 1110 °C. Grain boundaries are preserved and appear more curved than at lower temperature; and boundary bulging is clearly identified (Figure 4h). Together with a small decrease in GOS and weaker olivine CPO patterns, these observations suggest further activation of recovery mechanisms (subgrain boundary formation, grain boundary migration, ionic diffusion) than at lower temperature. This is consistent with recent values of Si diffusion in forsterite (Fei and Katsura, 2016), which, at 1200 °C, predict a strain rate of $\sim 10^{-5}$ s^{-1} for a grain size of 1 μm and a stress of ~500 MPa (Raj and Ashby 1971). Therefore, as already observed by Tasaka et al. (2013) under the same pressure, temperature and strain rate conditions, our experiment at 1200 °C also points to a transitional regime where both dislocation-accommodated grain boundary migration and diffusive mechanisms are active.

Conclusively, our results report a mechanical continuum from low temperature (i.e., semi-brittle) to high temperature plasticity. The temperature dependence of stress obtained at ≥ 1050 °C (Figure 11) is in agreement with that calculated from power law flow (e.g., Hirth and Kohlstedt, 2003; Ohuchi et al., 2015). Below 1050 °C, however, the temperature-dependence is greater than that calculated from exponential laws either from experimental studies (e.g., Evans and Goetze, 1979; Demouchy et al., 2013; Faul et al., 2011) or numerical modeling (Boioli et al., 2015b). As

detailed in the above, this is due to the occurrence of a variety of deformation mechanisms at play throughout the temperature range investigated.

Effect of iron on olivine strength

The stress values obtained in the present study are slightly larger (~17 and 50 % at 1000 and 1200 °C, respectively) than those reported for San Carlos olivine (Fo_{90}) aggregates in Thieme et al., (2018) using the same apparatus, under identical PT and strain rate conditions and with a comparable grain size (Figure 11), which is qualitatively consistent with the notorious weakening effect of iron on olivine (Bollinger et al., 2015; Zhao et al., 2009). The compositional effect observed here is weaker than the one reported by Zhao et al., (2009) at identical PT conditions, which predicts at least an order of magnitude increase in stress. However, their iron-content dependent rheology law was based on Fo_{00}-Fo_{90} compositions and the chosen expression is mathematically unfit to predict stress/strain values for Fo_{100} (strain rate nil for Fo_{100}). A direct rheological comparison between ion-bearing and iron-free olivine at high pressure (3.1-8.1 GPa) by Bollinger et al. (2015) has also reported weaker effects of iron incorporation. Following the approach of Bollinger et al., (2015, see their equation 3), i.e., using a power flow law and assuming constant activation energies and pre-exponential terms; the difference observed at 1200 °C can be explained by a stress exponent decrease from 3.5 for Fo_{90} olivine to only ~3.25 for Fo_{100} forsterite, whereas an exponent of 2.3 was found by Bollinger et al. (2015) at 1100-1300 °C and ~5 GPa. The present results thus point to a small rheological effect of iron (between Fo_{100} and F_{90}) on GBS in very fine-grained olivine aggregates.

Implications for the lithospheric mantle

In summary, the GBS observed in our samples in the brittle-ductile transition field (950-1050 °C) upon modest amounts of strain (<2 %), is first transiently accommodated elastically and then viscously. Upon further strain, GBS eventually produces significant cavitation. This reflects specific experimental conditions, namely (i) relatively low temperatures ($T/T_m \leq 0.68$), (ii) fast strain rates (10^{-5} s^{-1}) and (iii) sub-micron grain-sized and well annealed polygonal microstructures, which are all prerequisites to generate high macroscopic differential stress relative to confining pressure and induce cavitation without immediate failure of the samples. Such conditions may be achieved in mantle shear zones with peculiar settings, such as in tectonically exhumed mantle, where deformation at crustal pressure and temperatures may locally allow stress to exceed lithostatic pressure and, in turn, lead to GBS and gaping as observed in our experimental study. Under the present dry conditions, high local differential stresses are needed for cavitation to generate unpressurized voids (Burnley, 2013). However, cavitation may occur with lower stress levels if pressurized aqueous fluids or reactive melts are present (Précigout and Stünitz, 2016).

In addition, the predominance of diffusion creep or GBS over dislocation creep in mylonitic shear bands in peridotites is still debated based on field and microstructural evidences. It strongly depends on stress and strain rate evolution upon grain size reduction (Platt and Behr, 2011). On the other hand, the recent review of Vauchez et al. (2012) suggests that, in most instances, the dominant mechanism remains dislocation creep, associated to grains sizes of typically ~200 μm. In any case, in the lithospheric mantle, GBS and cavitation might be transient mechanisms occurring in incipient mantle shear zones in response to large stresses. Eventually, lower strain rates and stresses will likely allow ionic diffusion, rather than cavitation, to accommodate deformation.

5. Conclusions

(1) In the present experiments, several deformation mechanisms are at play with their respective contributions varying with temperature, and stress levels. We document a transition from micro-cracking to grain boundary sliding, and then to dislocation creep at around 1050-1100 °C; with a potential important contribution of ionic diffusion at 1200 °C.

(2) The transition results in subtle changes in SPO and CPO, but is evident in the recovered microstructures in SEM and TEM. Moreover, in our experiments, as well as in previous experimental studies, grains slide against their neighbors towards areas where, local tensile stresses have been generated by large stress heterogeneities. This is possible under moderate confining pressure in laboratory, where the Goetze criterion can be violated in a transient way.

(3) Given the experimental high-stress conditions, our results may not directly apply to the deformation of the Earth's mantle at large scale. Nevertheless, our results highlight that the grain boundary network in forsterite aggregates is an agent of deformation that is activated at lithospheric temperatures (< 1100 °C), before intracrystalline deformation.

6. Acknowledgments

The authors wish to thank Franck Nono, Manuel Thieme and Nicolas Marino for their valuable help running the Paterson press; Christophe Nevado and Doriane Delmas for providing high-quality polished crossed sections for EBSD-SEM; Julien Fauconnier for his assistance mastering some basic MATLAB knowledge. The authors also benefited from fruitful discussions with David Mainprice, Alain Vauchez, Andrea Tommasi and Benoit Ildefonse. The TEM and EBSD-SEM in Lille and Montpellier, respectively, are national facilities supported by the Institut National de Sciences de l'Univers (INSU), the Centre National de la Recherche Scientifique (CNRS, France), the Conseil Régional Occitanie (France), and the Conseil Régional du Hauts-de-France (France). This study was funded by the Agence Nationale de la Recherche through the INDIGO grant (ANR-14-CE33-0011). This study was supported by the JSPS KAKENHI grant (number

JP18K03799) to Sanae Koizumi and the cooperative research program of the Earthquake Research Institute, Tokyo (Japan). This is CRPG contribution n°2698.

7. References

Bachmann, F., Hielscher, R., Schaeben, H., 2010. Texture Analysis with MTEX - Free and Open Source Software Toolbox. Solid State Phenom. 160, 63–68. http://dx.doi.org/10.4028/www.scientific.net/SSP.160.63.

Boioli, F., Carrez, P., Cordier, P., Devincre, B., Marquille, M., 2015. Modeling the creep properties of olivine by 2.5-dimensional dislocation dynamics simulations. Phys. Rev. B 92, 014115.

Boioli, F., Tommasi, A., Cordier, P., Demouchy, S., Mussi, A., 2015. Low steady-state stresses in the cold lithospheric mantle inferred from dislocation dynamics models of dislocation creep in olivine. Earth and Planetary Science Letters 432, 232–242.

Bollinger C., Marquardt, K., and Ferreira F. (2019) Intragranular plasticity vs. grain boundary sliding (GBS) in forsterite: microstructural evidence at high pressures (3.5-5.0 GPa). American Mineralogist. 104 (2): 220-231.

Bollinger, C., Merkel, S., Cordier, P., Raterron, P., 2015. Deformation of forsterite polycrystals at mantle pressure: Comparison with Fe-bearing olivine and the effect of iron on its plasticity. Physics of the Earth and Planetary Interiors 240, 95-104.

Bunge, H.J., 1982. in: Butterworth-Heinemann (Ed.), Texture Analysis in Materials Science: Mathematical Methods, English Ed., 1st ed, p. 593.

Burnley, P.C., 2013. The importance of stress percolation patterns in rocks and other polycrystalline materials. Nature Comm. 4, 2117. Doi: 10.1038/ncomms3117

Burnley, P.C., Kaboli, S., 2019. Elastic plastic self-consistent (EPSC) modeling of San Carlos olivine deformed in a D-DIA apparatus. American Mineralogist 104, 276–281.

Cline, C.J., Faul, U.H., David, E.C., Berry, A.J., Jackson, I., 2018. Redox-influenced seismic properties of upper- mantle olivine. Nature 555, 355–358.

Cordier, P., Demouchy, S., Beausir, B., Taupin, V., Barou, F., Fressengeas, C., 2014. Disclinations provide the missing mechanism for deforming olivine-rich rocks in the mantle. Nature 507, 51-54.

Demouchy, S., Mainprice, D., Tommasi, A., Couvy, H., Barou, F., Frost, D.J., Cordier, P., 2011. Forsterite to wadsleyite phase transformation under shear stress and consequences for the Earth's mantle transition zone. Phys. Earth Planet. Int. 184, 91–104.

Demouchy, S., Mussi, A., Barou, F., Tommasi, A., Cordier, P., 2014. Viscoplasticity of polycrystalline olivine experimentally deformed at high pressure and 900 degrees C. Tectonophysics 623, 123-135.

Demouchy, S., Schneider, S.E., Mackwell, S.J., Zimmerman, M.E., Kohlstedt, D.L., 2009. Experimental deformation of olivine single crystals at lithospheric temperatures. Geophysical Research Letters 36.

Demouchy, S., Tommasi, A., Ballaran, T.B., Cordier, P., 2013. Low strength of Earth's uppermost mantle inferred from tri-axial deformation experiments on dry olivine crystals. Physics of the Earth and Planetary Interiors 220, 37-49.

595 Druiventak, A., Trepmann, C.A., Renner, J., Hanke, K., 2011. Low-temperature plasticity of olivine during
596 high stress deformation of peridotite at lithospheric conditions - An experimental study. Earth and
597 Planetary Science Letters 311, 199-211.

598 Evans, B., Goetze, C., 1979. The temperature variation of hardness of olivine and its implication for
599 polycrystalline yield stress. J. Geophys. Res. 84, 5505–5524.

600 Faul, U.H., Cline, C.J., II, David, E.C., Berry, A.J., Jackson, I., 2016. Titanium-hydroxyl defect-controlled
601 rheology of the Earth's upper mantle. Earth and Planetary Science Letters 452, 227–237.

602 Faul, U.H., Gerald, J.D.F., Farla, R.J.M., Ahlefeldt, R., Jackson, I., 2011. Dislocation creep of fine-grained
603 olivine. Journal of Geophysical Research-Solid Earth 116. B01203.
604 http://dx.doi.org/10.1029/2009JB007174.

605 Fei, H., Hegoda, C., Yamazaki, D., Wiedenbeck, M., Yurimoto, H., Shcheka, S., Katsura, T., 2012. High
606 silicon self-diffusion coefficient in dry forsterite. Earth and Planetary Science Letters 345, 95-103.

607 Fei, H., Katsura, T., 2016. Si and O self-diffusion in hydrous forsterite and iron-bearing olivine from the
608 perspective of defect chemistry. Physics and Chemistry of Minerals 43, 119-126.

609 Frost, H.J., Ashby, M.F., 1982. Deformation mechanism maps: the plasticity and creep of metals and
610 ceramics. Pergamon press, oxford.

611 Gouriet K., Cordier P., Garel F., Thoraval C., Demouchy S., Tommasi A., Carrez P., 2019. Dislocation
612 Dynamics modelling of the power-law breakdown in olivine single crystals: toward a unified creep
613 law for the upper mantle. Earth Planet. Sci. Lett. 506, 282-291.

614 Hansen, L.N., Zimmerman, M.E., Kohlstedt, D.L., 2012. The influence of microstructure on deformation
615 of olivine in the grain boundary sliding regime. J. Geophys. Res. 117. B09201,
616 doi:10.1029/2012JB009305.

617 Hielscher, R., Schaeben, H., 2008. A novel pole figure inversion method: specification of the MTEX
618 algorithm. Journal of Applied Crystallography 41, 1024-1037.

619 Hiraga, T., Miyazaki, T., Yoshida, H., Zimmerman, M.E., 2013. Comparison of microstructures in
620 superplastically deformed synthetic materials and natural mylonites: Mineral aggregation via grain
621 boundary sliding. Geology 41, 959-962.

622 Hirth, G., Kohlstedt, D.L., 2003. Rheology of the upper mantle and the mantle wedge: a view from the
623 experimentalists, in: Inside The Subduction Factory. American Geophysical Union, Washington
624 D.C., pp. 83–105.

625 Huet, B., P. Yamato, and B. Grasemann (2014), The Minimized Power Geometric model: An analytical
626 mixing model for calculating polyphase rock viscosities consistent with experimental data, J.
627 Geophys. Res. Solid Earth, 119, 3897–3924, doi:10.1002/2013JB010453.

628 Idrissi, H., Bollinger, C., Boioli, F., Schryvers, D., Cordier, P., 2016. Low-temperature plasticity of olivine
629 revisited with in situ TEM nanomechanical testing. Science Advances 2, e1501671.

630 Ji S., Wang, Z., Wirth, R., 2001. Bulk flow strength of forsterite–enstatite composites as a function of
631 forsterite content. Tectonophysics, 341, 69-93.

632 Kohlstedt, D.L., Evans, B., Mackwell, S.J., 1995. Strength of the lithosphere: Constraints imposed by
633 laboratory experiments. J. Geophys. Res. 100, 17–587–17–602.

634 Koizumi, S., Hiraga, T., Tachibana, C., Tasaka, M., Miyazaki, T., Kobayashi, T., Takamasa, A., Ohashi, N.,
635 Sano, S., 2010. Synthesis of highly dense and fine-grained aggregates of mantle composites by
636 vacuum sintering of nano-sized mineral powders. Physics and Chemistry of Minerals 37, 505-518.

637 Langdon, T.G., 2006. Grain boundary sliding revisited: Developments in sliding over four decades.
638 Journal of Materials Science 41, 597-609.

639 Mackwell, S.J., Kohlstedt, D.L., Paterson, M.S., 1985. The role of water in the deformation of olivine
640 single crystals. J. Geophys. Res. 90, 11–319–11–333.

641 Mainprice, D., Bachmann, F., Hielscher, R., Schaeben, H., 2015. Descriptive tools for the analysis of
642 texture projects with large datasets using MTEX: strength, symmetry and components. Rock
643 Deformation from Field, Experiments and Theory: a Volume in Honour of Ernie Rutter 409, 251-
644 271.

645 Mainprice, D., Tommasi, A., Couvy, H., Cordier, P., Frost, D.J., 2005. Pressure sensitivity of olivine slip
646 systems and seismic anisotropy of Earth's upper mantle. Nature 433, 731-733.

647 Maruyama, G., Hiraga, T., 2017a. Grain- to multiple-grain-scale deformation processes during diffusion
648 creep of forsterite plus diopside aggregate: 1. Direct observations. Journal of Geophysical Research-
649 Solid Earth 122, 5890-5915.

650 Maruyama, G., Hiraga, T., 2017b. Grain- to multiple-grain-scale deformation processes during diffusion
651 creep of forsterite plus diopside aggregate: 2. Grain boundary sliding-induced grain rotation and its
652 role in crystallographic preferred orientation in rocks. Journal of Geophysical Research-Solid Earth
653 122, 5916-5934.

654 Masuda, H., Tobe, H., Sato, E., Sugino, Y., Ukai, S., 2015. Mantle region accommodating two-dimensional
655 grain boundary sliding in ODS ferritic steel. Philosophical Mag Lett.
656 http://dx.doi.org/10.1080/09500839.2015.1067732

657 Masuda, H., Tobe, H., Sato, E., Sugino, Y., Ukai, S., 2016. Two-dimensional grain boundary sliding and
658 mantle dislocation accommodation in ODS ferritic steel. Acta Materialia 120, 205–215.

659 Mei, S., Kohlstedt, D.L., 2000. Influence of water on plastic deformation of olivine aggregates 2.
660 Dislocation creep regime. J. Geophys. Res. 105, 471–481.

661 Mei, S., Suzuki, A.M., Kohlstedt, D.L., Dixon, N.A., Durham, W.B., 2010. Experimental constraints on
662 the strength of the lithospheric mantle. Journal of Geophysical Research-Solid Earth 115. B08204,
663 doi:10.1029/2009JB006873.

664 Michibayashi, K., Mainprice, D., Fujii, A., Uehara, S., Shinkai, Y., Kondo, Y., Ohara, Y., Ishii, T., Fryer, P.,
665 Bloomer, S.H., Ishiwatari, A., Hawkins, J.W., Ji, S.C., 2016. Natural olivine crystal-fabrics in the
666 western Pacific convergence region: A new method to identify fabric type. Earth and Planetary
667 Science Letters 443, 70-80.

668 Nakakoji, T., Hiraga, T., Nagao, H., Ito, S., Kano, M., 2018. Diffusion creep and grain growth in forsterite
669 + 20 vol% enstatite aggregates: 1. High resolution experiments and their data analyses. J. Geophys.
670 Res: Solid Earth 123(11). doi: 10.1029/2018jb015818

671 Ohuchi, T., Nishihara, Y., Seto, Y., Kawazoe, T., Nishi, M., Maruyama, G., Hashimoto, M., Higo, Y.,
672 Funakoshi, K., Suzuki, A., Kikegawa, T., Irifune, T., 2015. In situ observation of crystallographic
673 preferred orientation of deforming olivine at high pressure and high temperature. Physics of the
674 Earth and Planetary Interiors 243, 1-21.

675 Paterson, M.S., 1990. Rock Deformation Experimentation, in: Duba, A.G., Durham, W.B., Handin, J.W.,
676 Wang, H.F. (Eds.), The Brittle-Ductile Transition in Rocks, pp. 187-194.

677 Phakey, P., Dollinger, G., Christie, J., 1972. Transmission Electron Microscopy of Experimentally
678 Deformed Olivine Crystals, in: H. C. Heard, I.Y.B., N.L. Carter, C. B. Raleigh (Ed.), Flow and
679 Fracture of Rocks.

680 Platt, J.P., Behr, W.M., 2011. Lithospheric shear zones as constant stress experiments. Geology. 39, 127-
681 130.

682 Ponson, L., Cao, Y., Bouchaud, E., Tvergaard, V., Needleman, A., 2013. Statistics of ductile fracture
683 surfaces: the effect of material parameters. Int J Fract 184, 137–149.

684 Précigout, J., Stünitz, H., 2016. Evidence of phase nucleation during olivine diffusion creep: A new
685 perspective for mantle strain localization. Earth and Planetary Science Letters 455, 94-105. doi:
686 10.1016/j.epsl.2016.09.029

687 Raj, R., Ashby, M.F., 1971. On grain boundary sliding and diffusion creep. Metal. Trans. 2, 1113–1127.

688 Raleigh, C.B., 1968. Mechanism of plastic deformation of olivine. J. Geophys. Res. 73, 5391–5406.

689 Ree, J.H., 1994. Grain boundary sliding and development of grain boundary opening in experimentally
690 deformed octachloropropane. J. Struct. Geol. 16, 403–418.

691 Suzuki, I., Anderson, O.L., Sumino, Y., 1983. Elastic Properties of a Single-Crystal Forsterite Mg2SiO4, up to 1,200
692 K. Phys Chem. Minerals, 10-38-46.

693 Tasaka, M., Hiraga, T., Zimmerman, M.E., 2013. Influence of mineral fraction on the rheological properties of
694 forsterite plus enstatite during grain-size-sensitive creep: 2. Deformation experiments. Journal of
695 Geophysical Research-Solid Earth 118, 3991-4012.

696 Tasaka, M., Zimmerman, M.E., Kohlstedt, D.L., 2016. Evolution of the rheological and microstructural properties
697 of olivine aggregates during dislocation creep under hydrous conditions. J. Geophys. Res. Solid Earth, 121,
698 92–113, doi:10.1002/2015JB012134.

699 Thieme, M., Demouchy, S., Mainprice, D., Barou, F., Cordier, P., 2018. Stress Evolution and Associated
700 Microstructure During Transient Creep of Olivine at 1000-1200°C. Physics of the Earth and Planetary
701 Interiors 278, 34-46.

702 Tielke, J. A., M. E. Zimmerman, and D. L. Kohlstedt 2017. Hydrolytic weakening in olivine single crystals, J.
703 Geophys. Res. Solid Earth, 122, 3465–3479, doi:10.1002/2017JB014004.

704 Tommasi, A., Mainprice, D., Canova, G., Chastel, Y., 2000. Viscoplastic self-consistent and equilibrium-based
705 modeling of olivine lattice preferred orientations: Implications for the upper mantle seismic anisotropy.
706 Journal of Geophysical Research-Solid Earth 105, 7893-7908.

707 Vauchez, A., Tommasi, A., Mainprice, D., 2012. Faults (shear zones) in the Earth's mantle. Tectonophysics 559-
708 559, 1-27.

709 Wallis, D., Hansen, L.N., Ben Britton, T., Wilkinson, A.J., 2016. Geometrically necessary dislocation densities in
710 olivine obtained using high-angular resolution electron backscatter diffraction. Ultramicroscopy 168, 34-45.

711 Watanabe, T., Obata, M., Karashima, S., 1982. High temperature intergranular fracture enhanced by grain
712 boundary migration in the alpha iron-tin alloy. In Strength of metal and alloys, ICSMA 6, Eds:
713 Taplin vol 1, 671-676, Pergamon Press.

714 Wheeler, J., 2018. The effects of stress on reactions in the Earth: Sometimes rather mean, usually normal, always
715 important. Journal of Metamorphic Geology 36, 439-461.

716 Zhao, Y.-H., Zimmerman, M.E., Kohlstedt, D.L., 2009. Effect of iron content on the creep behavior of
717 olivine: 1. Anhydrous conditions. Earth and Planetary Science Letters 287, 229-240.

718

Figures

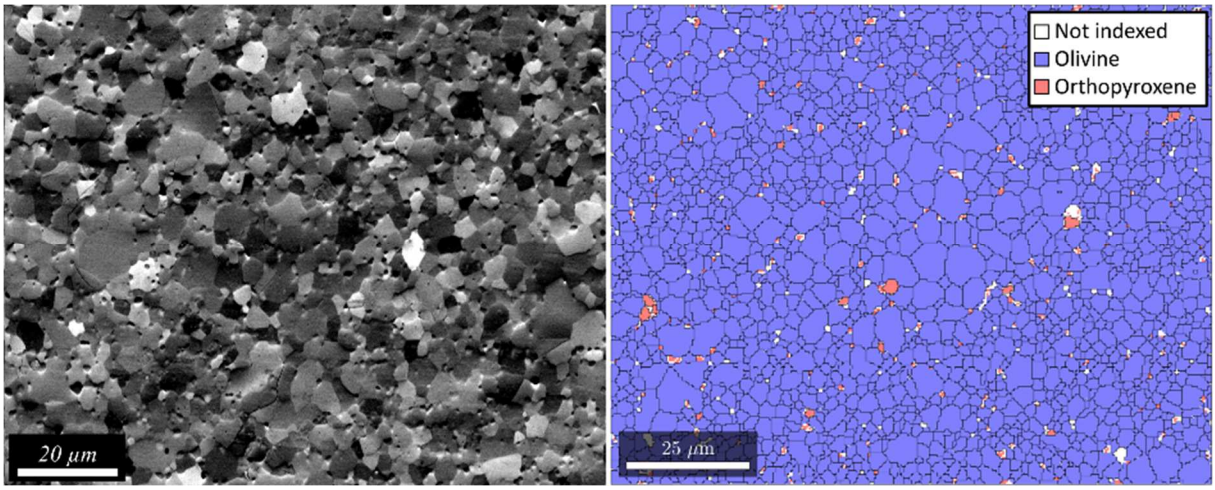

Figure 1: (a) SEM image (Forward scattered electrons) of the starting material used for the deformation experiments. (b) EBSD map collected on the same starting material showing phase distribution and grain boundaries determined with MTEX (black lines, see text for details).

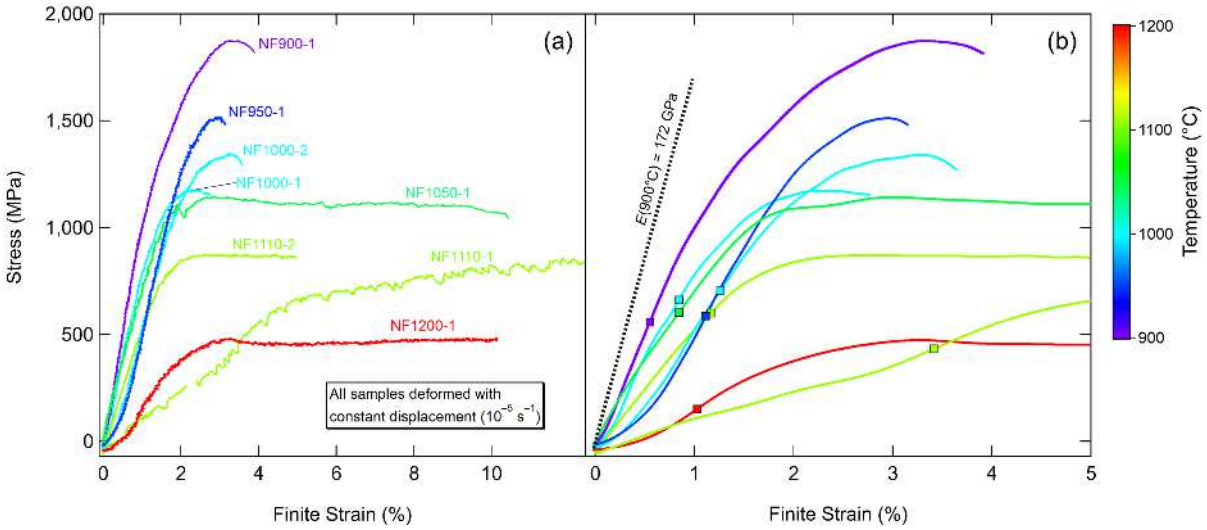

Figure 2: Stress-strain curves for axial deformation experiments. Each curve is colored as a function of temperature, according to the appended color scale. (a) Mechanical curves after data treatment (see section 2.2 for details). (b) Smoothed stress-strain curves (up to 5% strain) used to retrieve yield points, indicated by squares (see supp. mat. for details). As a guide to the eye, the Young modulus of forsterite at 900°C (172 GPa), calculated using the data of Suzuki et al. (1983), is also shown next to the data of NF_900-1, for which the apparent Young modulus is 112.2 GPa.

734

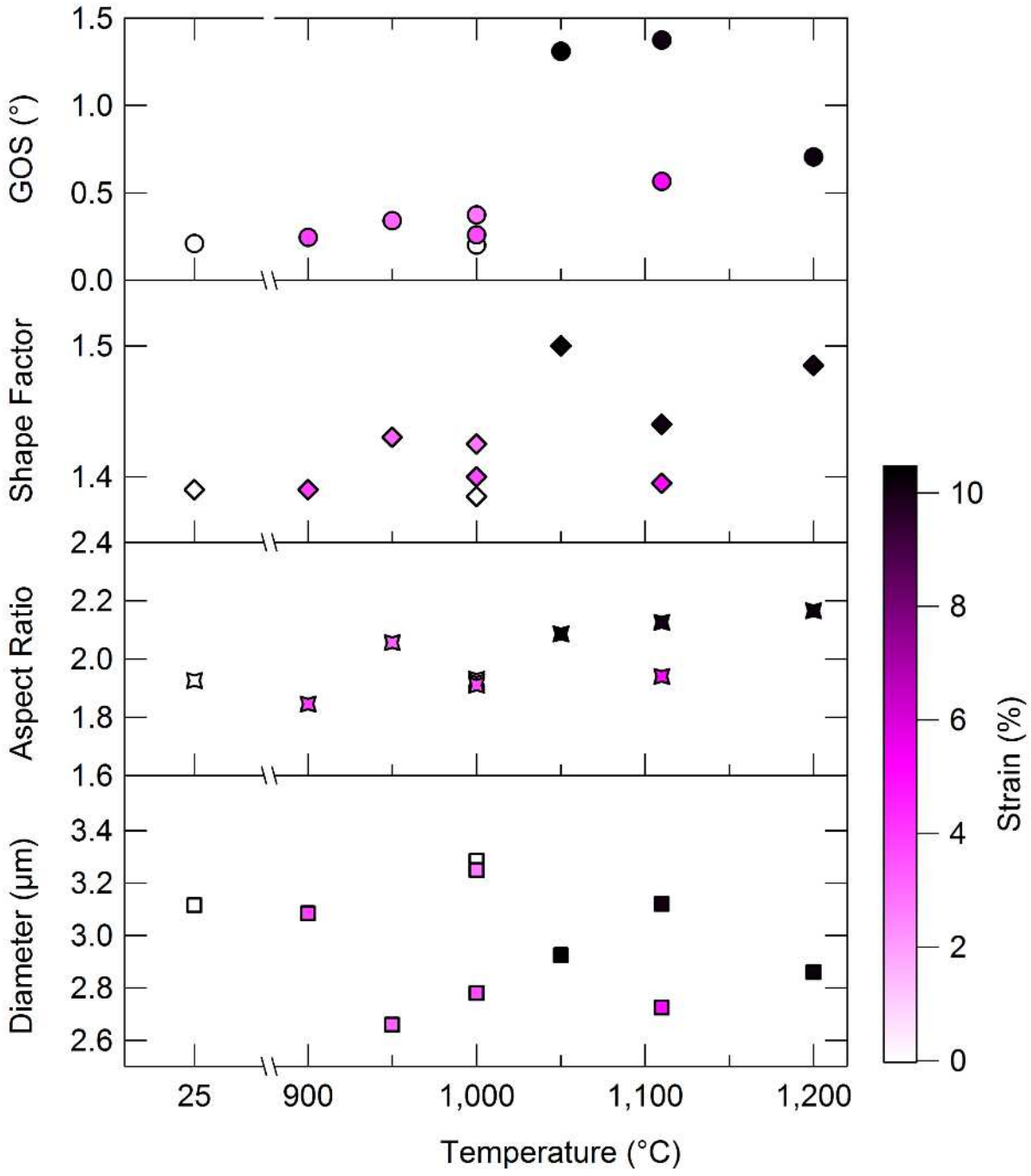

735

736 Figure 3: Grain size, shape parameters (shape factor and aspect ratio) and grain orientation spread (GOS)
737 as a function of temperature and finite strain. The leftmost datum point at room temperature and no strain
738 corresponds to the starting material. The other nine data points correspond to the static annealing test
739 (1000 °C, no strain) and the axial deformation experiments.

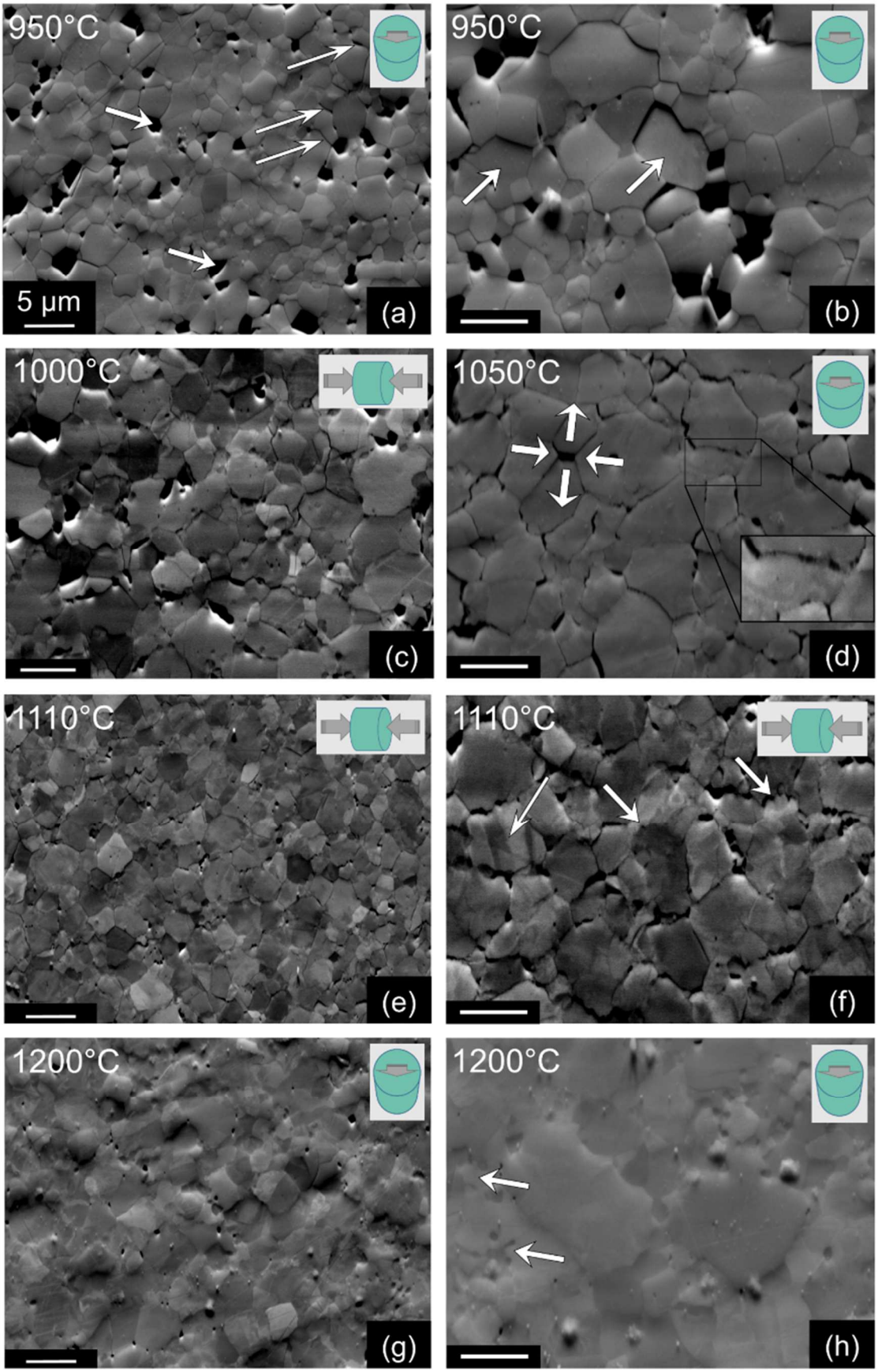

Figure 4: SEM images (forward scattered electrons) of samples deformed at various temperatures. Scale bar is 5 µm on all images. The direction of the deformation (either horizontal or in-plane) is given by the

743 schematic drawing in the top right corner of each image. (a) NF_950-1, 3.1% finite strain. Gaping grain
744 boundaries (thin white arrows) and grain plucking due to cross-section preparation (thick white arrows) are
745 visible. (b) NF_950-1. Arrows point at two grains, which show a significant vertical offset, as evidenced by
746 the shadows on the top of the grains. (c) NF_1000-2, finite strain of 3.6%. (d) NF_1050-1, finite strain of
747 10.4 %. The inset is a higher-magnification image with enhanced contrast that better shows serrated grain
748 boundaries. The white arrows depict relative grain motion, which has left a void between pulled-apart grains.
749 (e) NF_1110-2, finite strain of 5 %. (f) NF_1110-1, finite strain of 12.41 %. Thick arrows show serrated
750 grain boundaries, which have been characterized in detail with TEM (see below for more details). The
751 thinner arrow indicates a grain where bands with variable contrast highlight subgrain boundaries and thus
752 intracrystalline plasticity. (g) NF_1200-1, finite strain of 10 %. (h) NF_1200-1. Arrows show migrating (i.e.,
753 bulging) grain boundaries.

754

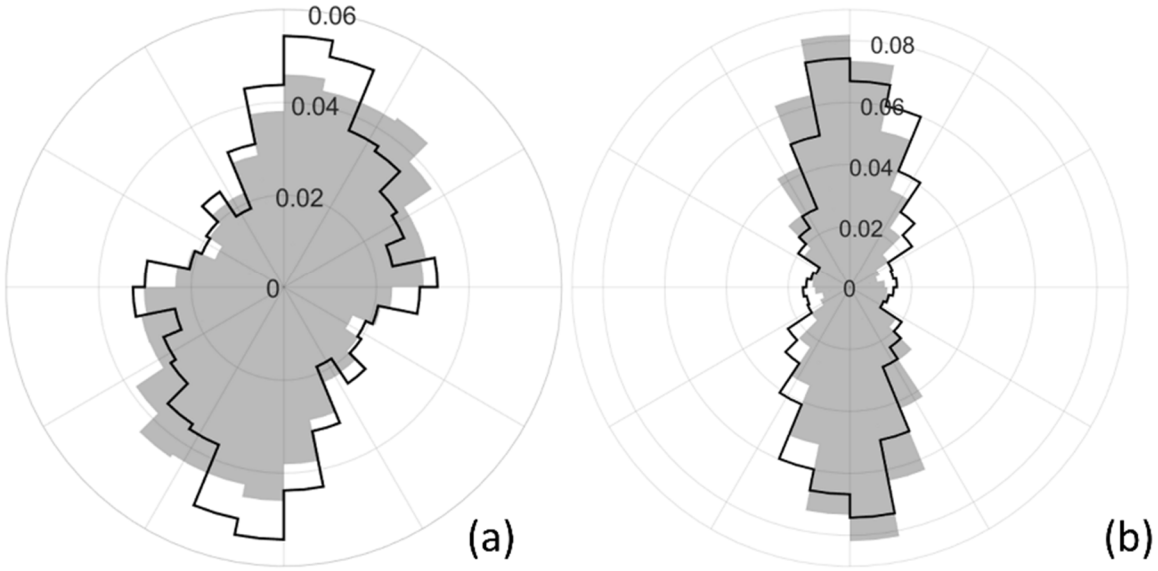

Figure 5: Polar histograms displaying the normalized orientation distribution of the longest axis of forsterite grains. Samples length, and therefore axial compression direction, is horizontal. (a) Starting material (black line) and sample NF_900-1 (grey bars), deformed to a finite strain of 3.9 %. (b) Samples NF_1110-2 (black line) and NF_1110-1 (grey bars) deformed by 5 and 12.41 % of finite strain, respectively.

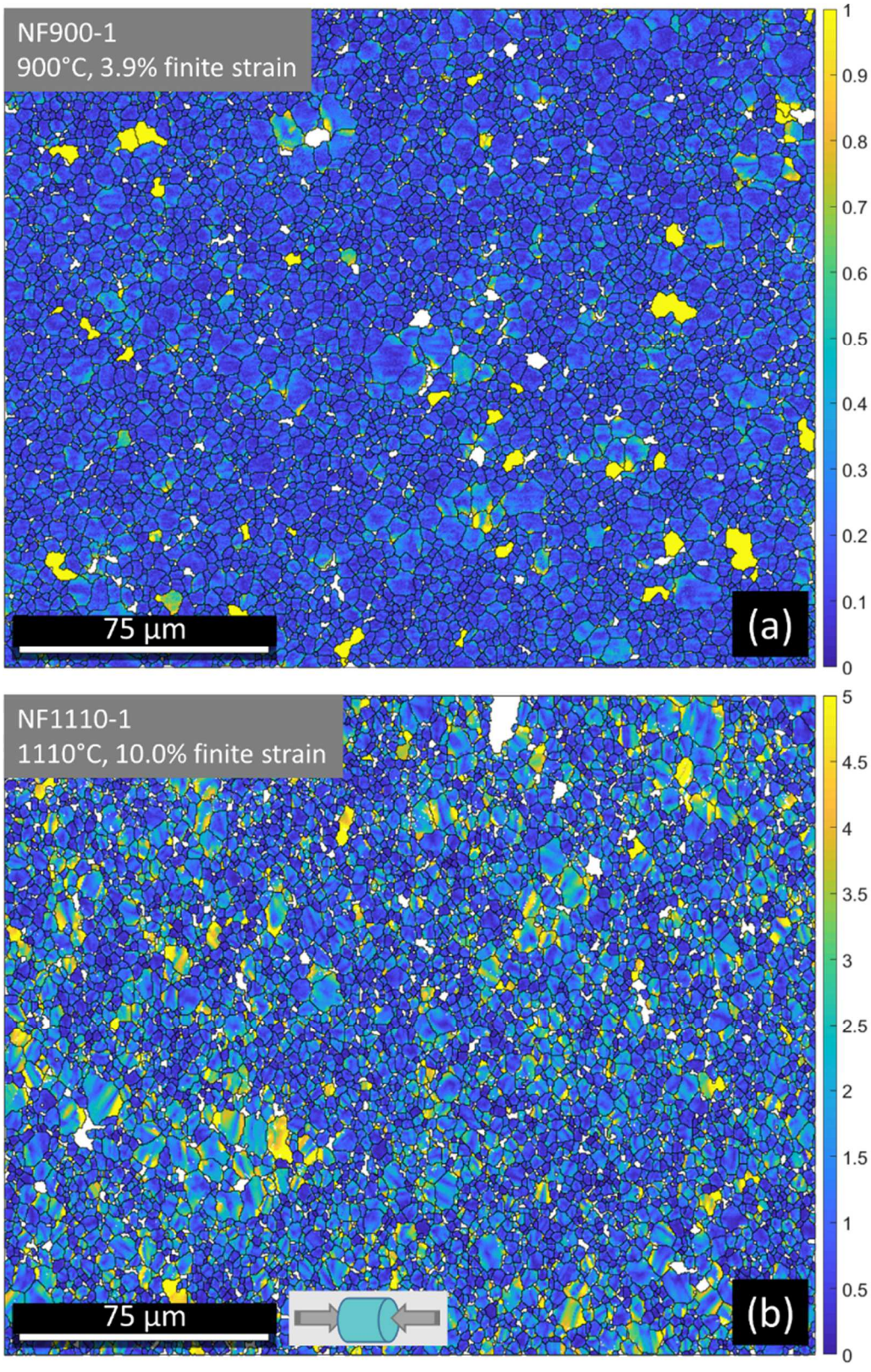

Figure 6: EBSD maps showing grain boundaries and Mis2Mean angles (°) within each grain. (a) Sample NF_900-1 (3.9 % finite strain). Very limited grain plasticity is observed, as shown by Mis2Mean values, which rarely exceed 1°. (b) Sample NF_1110-1 (12.41 % finite strain), which presents the largest GOS values observed in our samples. Note that the color scale maximum in (b) is five times larger than in (a).

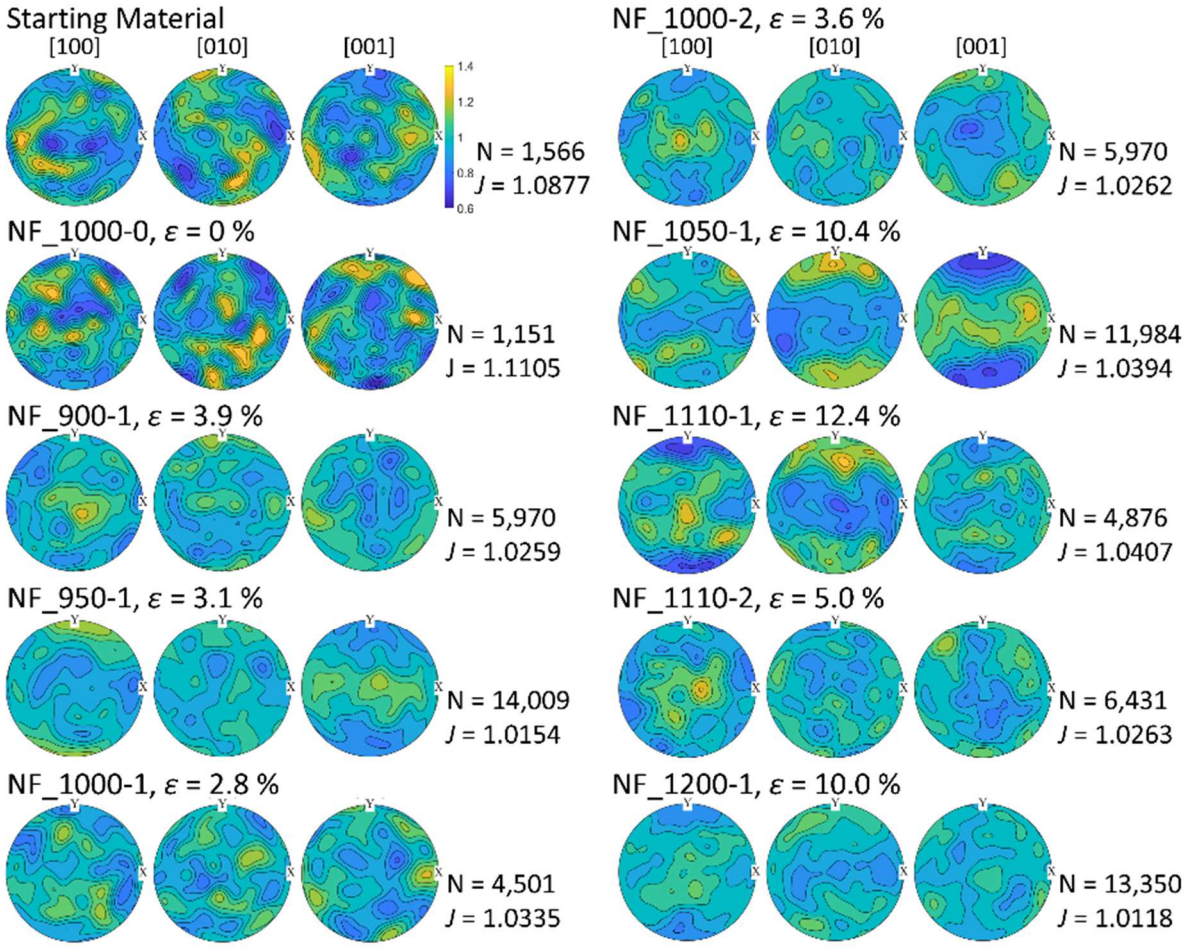

Figure 7: Pole figures of forsterite obtained for the starting material, the annealing experiment and each axial deformation experiment. Densities were obtained from the largest EBSD map collected on each sample and reduced to one point per grain. Densities were contoured with a 0.06 interval. The color scale given beside the starting material pole figures is the same on all figures. The number of grains used, N, and the corresponding J-index are provided in each case. The direction of axial compression deformation is vertical for all figures, except for sample NF_900-1, where orientation was lost due brittle failure of the sample.

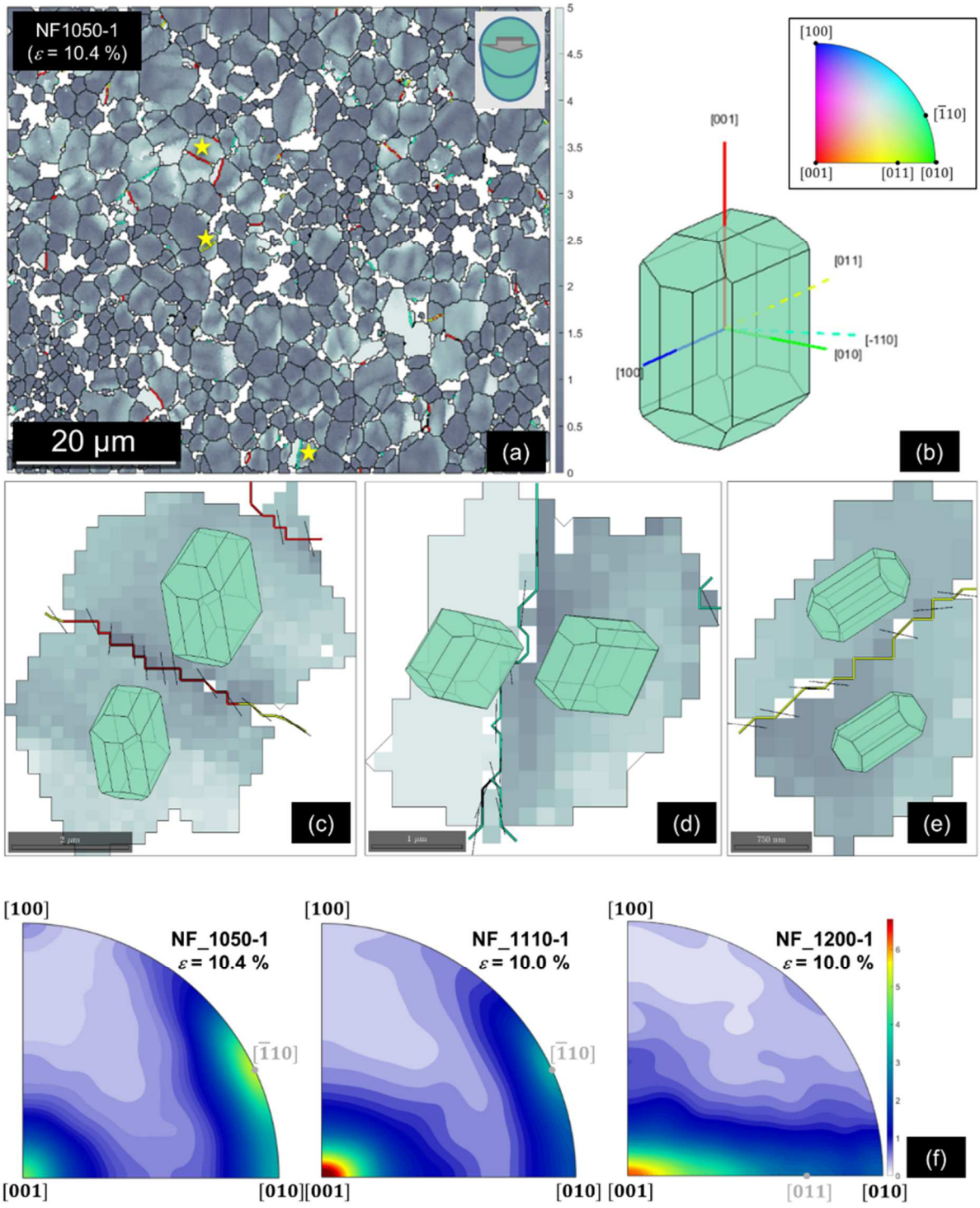

773

774 Figure 8: Intracrystalline plasticity at 1050-1200 °C. (a)-(e) Misorientation analysis in sample NF_1050-1. (a)
775 EBSD map showing Mis2Mean values, grain boundaries (black lines) and subgrain boundaries (thick colored
776 lines). (b) Reference forsterite crystal habitus used in (c), (d) and (e). In addition to principal axes, specific
777 axes, corresponding to $[\bar{1}10]$ and [011] subgrain rotations, are shown and colored according to the inverse
778 pole figure colors given in the inset. (c)-(e) Detailed views of grains (and subgrains) marked by a star in (a).
779 The bars on top of the subgrain boundaries represent the orientation of the subgrain rotation axis; their
780 length is a function of their dipping angle (i.e., they are shorter when the rotation axis sticks out of plane).

781 Similar figures for samples NF_1110-1 and NF_1200-1 are provided in the supplementary material (Figures
782 S3 and S4). (f) Inverse pole figures displaying the densities of subgrains rotation axes for samples NF_1050-
783 1, NF_1110-1 and NF_1200-1. The color scale gives the axis density. The majority of subgrain rotations
784 occur around the [001] and $[\bar{1}10]$ axis, and occasionally around the [011] axis; this latter case being more
785 common in sample NF_1200-1.

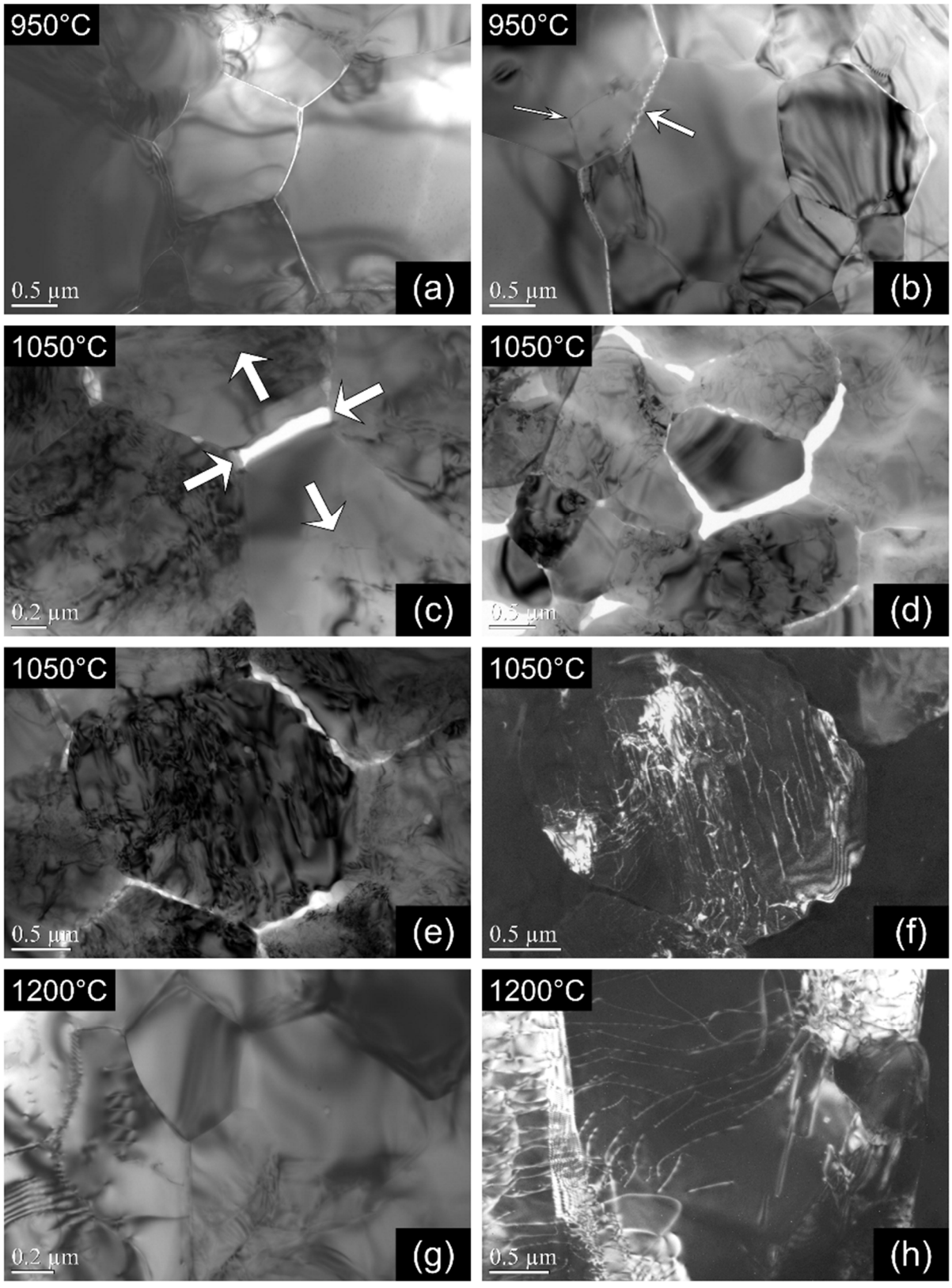

Figure 9: TEM images of samples deformed at 950-1200 °C. (a)-(b) Sample NF_950-1. (a) Grains show few to no dislocation. Gaping grain boundaries are straight, typical of brittle failure. (b) Several grain boundaries are serrated at the scale of a few tens of nanometers (thick arrow) and intragranular cracks are also present (thin arrow). A higher magnification image of these features is provided in the supplementary material

(Figure S6a). (c)-(f) Sample NF_1050-1. (c) Similar to SEM observations, cavitation and relative grain motion (white arrows) is observed. (d) In most cases the voids created upon deformation leave a mismatch between the grains pulled apart, i.e., the void cannot be closed by simply bringing the grains back together, thus suggesting a role of intracrystalline plasticity. (e) Opened grain boundaries are serrated at a larger scale. (f) Dark field imaging of the same grain reveals a high dislocation density. (g)-(h) Sample NF_1200-1. (g) Grain boundaries remained closed and, in certain areas, grains are pristine and almost dislocation free. (h) Dark field image in another area, where grains reveal high dislocation densities. Dislocation sources (loops) are visible in the middle lower part of the image.

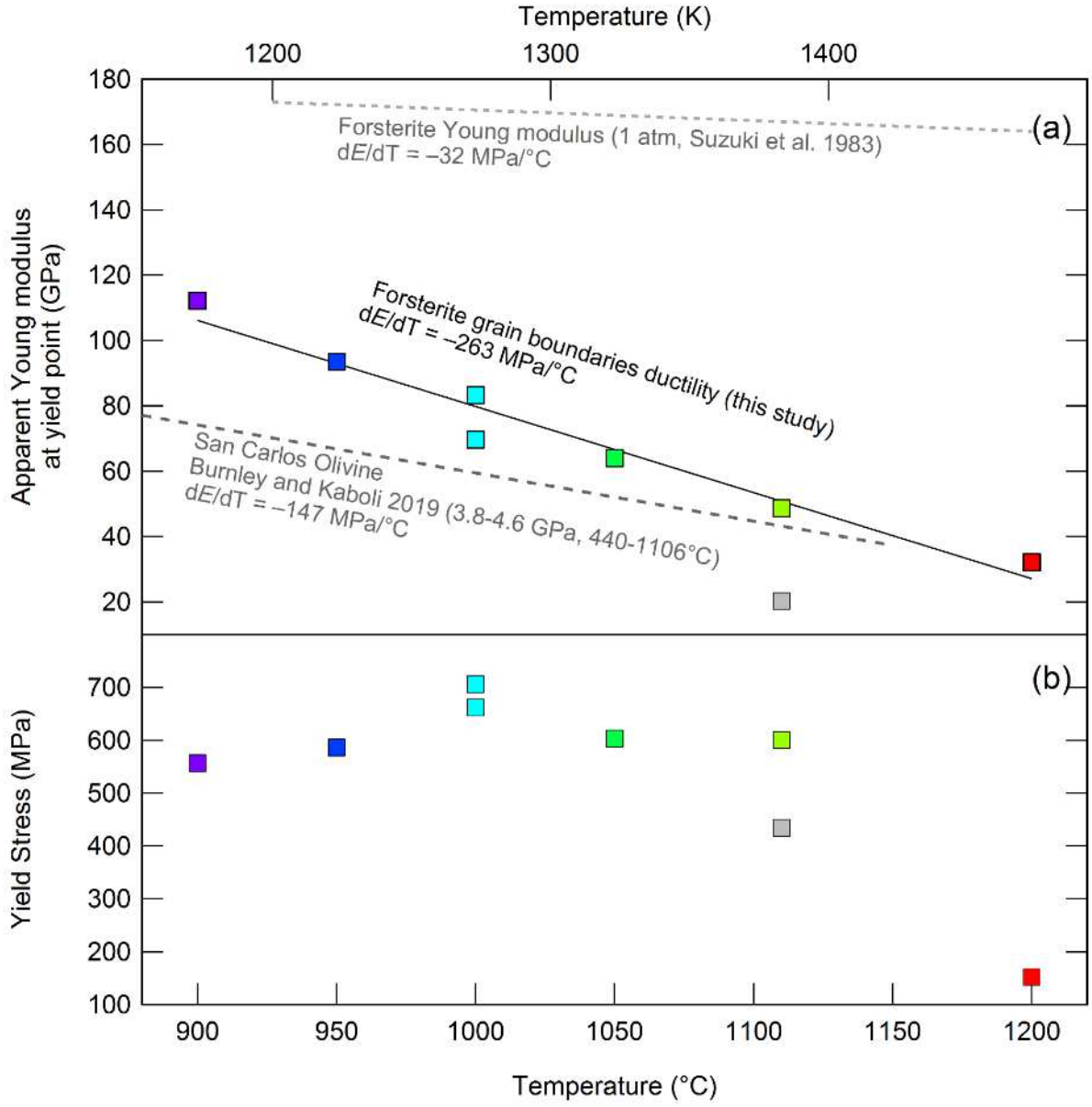

Figure 10: (a) Apparent Young modulus at yield point as a function of temperature. Young modulus of forsterite as a function of temperature from Suzuki et al. (1983) is shown for comparison. Values of grain boundaries apparent elasticity for iron-bearing olivine from Burnley and Kaboli (2019) are also reported. (b) Yield stress as a function of temperature from the mechanical curves displayed in Figure 2b (see Supp Mat for details, Figure S2).

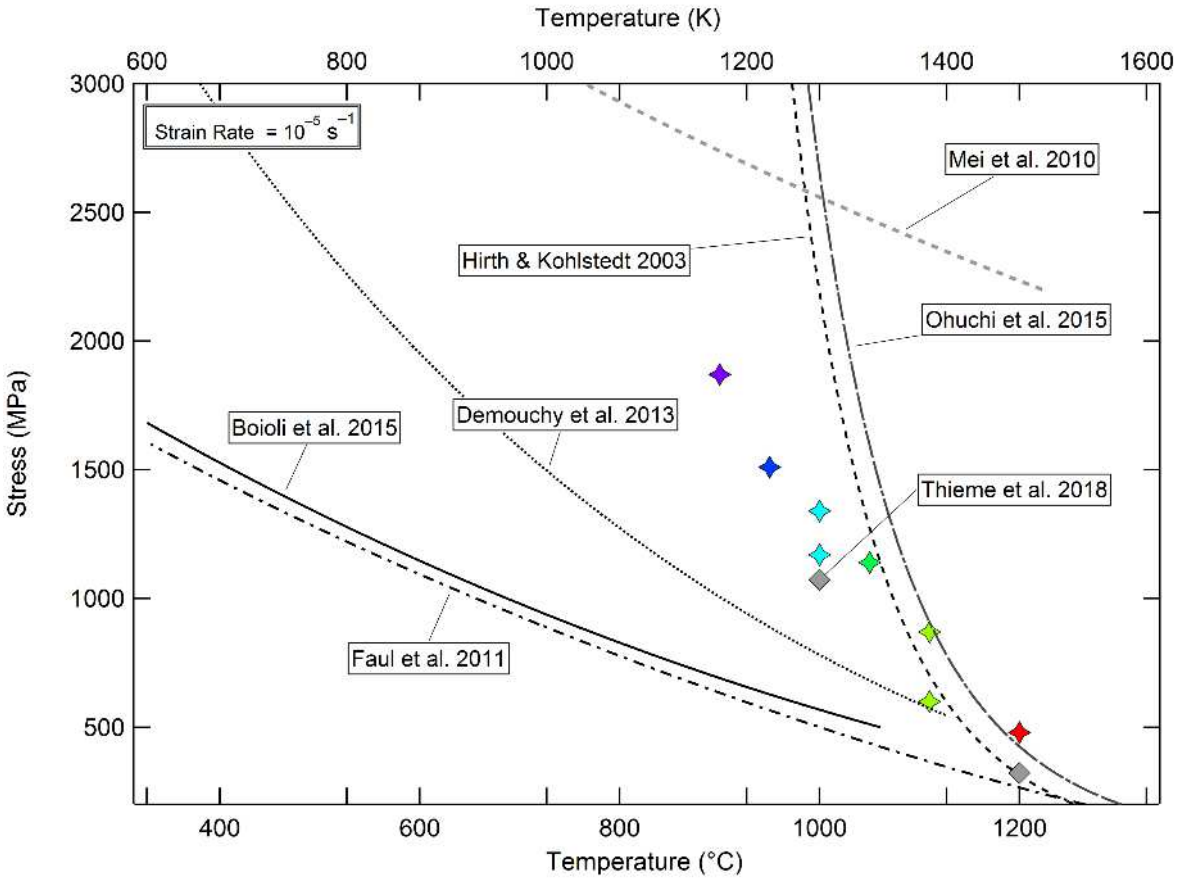

Figure 11: Comparison of iron-bearing olivine strength from the literature with the mechanical data from this study obtained on forsterite. All data are for a strain rate of 10^{-5} s^{-1}. The data points were colored as a function of temperature, according to same color scale used in Figure 2.

		Starting Material		**Static Annealing**		**Deformation Experiments**																	
	Sample Name	SM		NF1000-0		NF900-1		NF950-1		NF1000-1		NF1000-2		NF1050-1		NF1110-1		NF1110-2		NF1200-1	
Experimental Conditions and Results	**Temperature (°C)**	NA		1,000		900		950		1,000		1,000		1,050		1,110		1,110		1,200	
	Sleeve Type	NA		Ag		Ag		Ag		Cu		Cu		Cu		Ni		Ni		Ni	
	Initial Length (mm)	NA		NA		7.25		10.20		10.35		9.60		10.55		10.42		9.48		10.35	
	Strain (%)	NA		NA		3.9		3.1		2.8		3.6		10.4		12.4		5.0		10.0	
	Duration (s)	NA		14,400		9,308		6,502		5,154		8,198		12,668		14,024		6,917		11,022	
	Max Strength (MPa)	NA		NA		1,870		1,510		1,170		1,340		1,140		840		870		480	
	Yield Stress (MPa)	NA		NA		557		586		662		706		603		434		600		152	
	Apparent *E* at Yield (GPa)	NA		NA		112.2		93.5		83.2		69.6		63.9		20.2		48.6		32.1	
EBSD Analysis	**# Grains**	1,566	1,035	1,151	1,077	4,625	5,970	1,544	14,009	4,501	4,185	5,970	1,564	11,984	823	4,876	4,628	6,431	6,054	13,350	951
	***J* index**	1.1637	1.2680	1.2526	1.2472	1.0618	1.0509	1.1838	1.0236	1.0782	1.0871	1.04881	1.1568	1.0532	1.3567	1.0657	1.082	1.0449	1.0432	1.02335	1.3568

	***J* index 1PPG**	1.0877	1.1285	1.1105	1.1335	1.0314	1.0259	1.0949	1.0154	1.0335	1.0364	1.02662	1.0857	1.0394	1.2434	1.0407	1.0453	1.0263	1.0246	1.01118	1.1569
	Average Grain Size (µm)	3.115		3.285		3.085		2.660		3.250		2.780		2.925		3.120		2.725		2.860	
	Mean Aspect Ratio	1.925		1.930		1.845		2.055		1.920		1.910		2.085		2.125		1.940		2.165	
	Mean Shape Factor	1.390		1.385		1.390		1.430		1.425		1.400		1.500		1.440		1.395		1.485	
	Mean GOS (°)	0.210		0.200		0.245		0.340		0.375		0.260		1.310		1.375		0.565		0.705	